



STScI | SPACE TELESCOPE
SCIENCE INSTITUTE

Instrument Science Report WFC3 2023-02

Testing Aperture Corrections for WFC3/UVIS Spatial Scans

Mariarosa Marinelli & Varun Bajaj

May 1, 2023

ABSTRACT

For the absolute flux calibration of the WFC3/UVIS detector, the aperture-corrected photometry of standard stars observed in staring mode is compared to the predicted photometry of simulated observations. Spatial scans offer greater precision than staring mode observations, but currently cannot be used directly for the absolute calibration of the instrument, as existing software used for generating synthetic observations lacks the capacity to model rectangular photometric apertures used for spatial scans. In this report, we introduce a novel method for calculating aperture corrections for spatial scans, and present the results of preliminary tests of this methodology. We find that ratios of observed-to-synthetic flux are constant over time, validating the implementation of current time-dependent zeropoints. However, the data exhibits a wavelength- and chip-dependent offset between observed and synthetic count rates. This offset may be due to underlying factors complicating the observed photometry, aperture corrections, or both. Until this discrepancy is resolved, spatial scans will not be directly used for the photometric calibration of the WFC3/UVIS instrument. Meanwhile, we provide calculated offset values for each chip and filter as evidence of our initial efforts. A future report will utilize deep exposures from an upcoming calibration program (Program 17271) to examine encircled energies at large radii in order to further refine the process of calculating aperture corrections for spatial scans.

Contents

1. Introduction	3
2. Data	5
2.1. CTE	5
2.2. Photometry	6
3. Methods	8
3.1. Aperture Corrections	8
3.1.1 Point Spread Functions (PSFs)	8
3.1.2 Scan Spread Functions (SSFs)	9
3.1.3 Calculating Enrectangled Energy Fractions	9
3.2. Synthetic Photometry	12
4. Analysis	13
4.1. Applying Aperture Corrections	13
4.2. Effect of Aperture Width	14
5. Results	15
6. Discussion	20
7. Conclusions	20
Acknowledgements	21
References	21

1. Introduction

WFC3 has two primary observational modes - staring mode and spatial scans. In staring mode, guide star acquisition and subsequent tracking ensures that the target remains in the same place on the CCD during the course of the observation. For spatial scans, the telescope moves in a prescribed trajectory after guide star acquisition, resulting in the flux from a given object being trailed across the detector (McCullough, 2017). Thus, in a spatial scan of a bright target, the exposure time to saturation is longer than for a staring mode observation.

Following up on preliminary results presented in Shanahan et al. (2017), in Marinelli et al. (2022), five years of WFC3/UVIS spatial scans of spectrophotometric standard stars were analyzed. The motivation for the 2022 report was two-fold: to assess the precision of spatial scans relative to staring mode observations, and to compare how observational mode and observation date affects the measurement of detector sensitivity changes over time ($\sim 0.1 - 0.2\%$ per year). In all seven wide-band filters¹ examined, and on both UVIS chips, scans yield higher precision photometry than staring mode observations, with the photometric scatter reduced by $2 - 5\times$, depending on filter. Scan-derived sensitivity loss rates, calculated from relative photometry, agreed within computed uncertainties with losses previously published (Calamida et al., 2021) as well as rates calculated only from staring mode observations.

However, that report solely utilized relative photometry, comparing the measured fluxes of scans over time in order to determine photometric sensitivity changes over time. For staring mode observations, the observed count rate for a given standard star is compared to a corresponding synthetic observation, calculated using spectral energy distributions (SEDs) available from CALSPEC and tied to the brightness of the star Vega at 5550 Å (Bohlin et al., 2020). The ratio between the observed count rate and synthetic count rate (hereafter referred to as the "obs-syn" ratio) allows us to calibrate WFC3/UVIS photometry, i.e. to provide inverse sensitivities (zeropoints) for different filters.

In order to measure the total count rate of a star, an aperture correction must be applied; this is because photometry on staring mode images is performed using a circular aperture of finite size, with a radius generally less than 20 pixels (≈ 0.8 arcsec). The flux encapsulated by this circular photometric aperture represents some fraction of the total flux, thus necessitating correction to the measured count rates within that aperture to account for the missing photons outside that aperture at some "infinite" aperture within which all flux is assumed to be contained. For WFC3/UVIS, that is currently assumed to be 150 pixels, or 6 arcsec, in radius. Aperture corrections for staring mode images are calculated by using observations of very bright stars in a few filters and then extrapolated to all WFC3/UVIS filters. The absolute flux calibration of WFC3/UVIS is then performed by using the corrected fluxes of standard stars, and comparing those to the aforementioned models.

Spatial scans pose a dilemma which has never been broached before: how do you use scan photometry to perform absolute flux instrument calibration? Since the addition of

¹F218W, F225W, F275W, F336W, F438W, F606W, and F814W

spatial scans of spectrophotometric standard stars to the WFC3 photometric calibration program roster, scans have always been used *indirectly* for the calculation of the slope of the UVIS time-dependent zeropoints. That is, relative photometry from scans is compared to relative photometry of staring mode observations to verify that the measured slopes between observation methods (rates of detector sensitivity change over time) are similar (Calamida et al., 2021). From there, only the staring mode observations are used to calculate and, if needed, update the detector inverse sensitivities. i.e. to perform WFC3 flux calibration. Historically, we have not been able to fully leverage the fact that spatial scans are more precise than staring mode observations (Marinelli et al., 2022, Shanahan et al., 2017) for the computation of WFC3/UVIS zeropoints.

A star observed in staring mode can be characterized by a point spread function (PSF). In contrast, the line of flux from scans is better characterized by what we will hereafter call a scan spread function (SSF). Hence, unlike the radially symmetric apertures used for staring mode photometry, we utilize long rectangular apertures for scan photometry so as to enclose the maximum amount of flux from the scan while minimizing noise contributions from the background and systematic errors due to uncertainties in the calibration reference files (post-flash, flat field, etc.). Moreover, existing software tools used to calculate synthetic observations, like the Python packages `synphot`² and `stsynphot`³ lack the capability to model non-circular photometric apertures, and therefore are not equipped to calculate aperture corrections that are not radially symmetric. This means we cannot directly compare the measured photometry of spatial scans (rectangular apertures) to synthetic photometry (circular apertures).

To address the disjunction between observing modes, Riess et al. (2018) dedicated additional observing time to taking a staring mode image for every scan observed. Utilizing these paired observations, an empirical offset between each observation mode’s photometry was measured for two UVIS filters (F555W and F814W) and one IR filter (F160W), thus effectively accounting for the aperture correction of their scanned observations. Unlike the methodologies of Shanahan et al. (2017) and Marinelli et al. (2022), Riess et al. (2018) measure scan photometry in 15-pixel “minirows” instead of rectangular apertures, a significant divergence between our procedures. Nonetheless, this outcome is promising and unsurprising, as the temporal sensitivity rate of the detector as measured by spatial scans has been found to align with the long-term rates derived purely from staring mode photometry (Marinelli et al., 2022).

With this in mind, we hypothesize that the difference in flux between the observing methods can be attributed to an aperture correction-like term. Deriving a generalizable procedure to correct spatial scan photometry to an infinite radius by calculating its enclosed energy would not only be a highly useful tool for instrument calibration and monitoring, but would also be helpful for observers leveraging high-precision spatial scans for science purposes. Most observers should not need to take their own biases, flats, or darks to calibrate their observations. Providing calibration resources for scan photometry could obviate the need for additional observing time dedicated to taking calibration images, and would expand

²`synphot` (Lim, 2020)

³`stsynphot` (Lim, 2018)

the usage and applicability of the observing method overall.

In this report, we introduce a novel method for calculating spatial scan aperture corrections, and we present the results of preliminary tests of this methodology.

We describe the processing and data reduction of spatial scans to yield catalogs of photometry in Section 2.. In Section 3., we detail the methods by which we constructed scan spread functions, computed “enrectangled” energy fractions, and calculated radially-symmetric (e.g. staring mode) synthetic photometry. In Section 4., we apply the aperture corrections to the ratio of observed to synthetic count rates. Impact of aperture width on enrectangled energy is also examined. Results are presented in Section 5., including wavelength-dependent systematic offsets and a brief examination of encircled energy at large radii. Finally, in Section 6., we discuss the implications of our findings, and situate them within a wider context of investigation into the behavior of the WFC3/UVIS PSF at large radii.

2. Data

This report makes use of the observational data published in Marinelli et al. (2022), in addition to new data from the Cycle 29 UVIS scan monitoring program (2021 - 2022).

Observational data published in Marinelli et al. (2022) were derived from five cycles of completed programs (2017 - 2021), and included observations of three discreet targets in a total of 12 different filters. However, only observations in a core group of seven filters⁴ were used for analysis in that report. Marinelli et al. (2022) also only examined the two white dwarf stars observed in every program, GD153 and GRW70. Observations with guidestar failure, excessive instrumental jitter, or of otherwise poor data quality were excluded as well. In this report, we additionally use data from the completed Cycle 29 UVIS scan monitoring program, while following the same strict set of inclusion restrictions.

2.1. CTE

To mitigate CTE losses, scan orientation, choice of subarray, and utilization of post-flash were all taken into consideration. Vertical scans were acquired with a scan angle of 90.3° to provide a 1-pixel lateral shift during a 190-pixel trail. Scans were done on the 512×512 subarrays UVIS1-C512A-SUB and UVIS2-C512C-SUB, located in the FOV corners nearest the readout amplifiers A and C, respectively. Initially (Cycles 24-26), scans on UVIS 2 alternated between no post-flash and a post-flash of 12 electrons; beginning in Cycle 27, and in accordance with updated observation recommendations, all scans on both CCDs were post-flashed (Anderson 2020; Anderson et al. 2021). A summary of the scan calibration programs acquired from 2017 through 2022 is presented in Table 1.

⁴F218W, F225W, F275W, F336W, F438W, F606W, and F814W

Program	Cycle	CCD	Post-flash (e-)	Targets	Filters
14878	24	UVIS 1	0	GD153, GRW70	F218W, F225W, F275W, F336W, F438W, F606W, F814W
		UVIS 2	0, 12		
15398	25	UVIS 1	0	GD153, GRW70	F218W, F225W, F275W, F336W, F438W, F606W, F814W
		UVIS 2	0, 12		
15583	26	UVIS 1	0	GD153, GRW70	F218W, F225W, F275W, F336W, F438W, F606W, F814W
		UVIS 2	0, 12		
16021	27	UVIS 1	12	GD153, GRW70, <i>P330E</i>	F218W, F225W, F275W, F336W, F438W, F606W, F814W, <i>F390W, F475W,</i> F555W, F625W, F775W
		UVIS 2	12		
16416	28	UVIS 1	20	GD153, GRW70, <i>P330E</i>	F218W, F225W, F275W, F336W, F438W, F606W, F814W, <i>F390W, F475W,</i> F555W, F625W, F775W
		UVIS 2	20		
16580	29	UVIS 1	20	GD153, GRW70, <i>P330E</i>	F218W, F225W, F275W, F336W, F438W, F606W, F814W, <i>F390W, F475W,</i> F555W, F625W, F775W
		UVIS 2	20		

Table 1: Observation information and varying parameters for completed programs using spatial scans for UVIS photometric monitoring. The target and filters that are not used in this analysis are italicized and included for completeness. Adapted from Table 1 of Marinelli et al. (2022). Note that the exposure time for every scan is set to 59.9 seconds, regardless of target or filter.

2.2. Photometry

Photometry was calculated in the following procedure:

- Fully calibrated scan files (FLTs) were visually inspected to ensure that no scans with observing errors were used (like observations affected by loss of guide star lock).
- Cosmic ray rejection was performed, flagging and interpolating problematic pixels. The resulting flat-fielded, cosmic-ray rejected files are hereafter referred to as FCRs.
- Geometric distortion, resulting in varying pixel area across the field of view (Kalirai et al., 2010), was corrected by applying the Pixel Area Map (PAM) to the FCRs.

- The sky background was calculated for each FCR, using a rectangular “rind” centered around the scan, as seen in the left side of Figure 1. This 30-pixel-wide rind had an inner boundary 300 pixels wide and 400 pixels tall, and an outer boundary 360 pixels wide and 460 pixels tall. This was deemed sufficiently far away from the scan to minimize the amount of diffuse light, originating from the scan itself, that is encapsulated in the rind used for calculating the background.
- We calculated the amount of flux inside an aperture 44 pixels wide and 268 pixels tall and subtracted the calculated sky background. This yields the count rate inside the rectangular aperture.

Basic analysis was then performed on the photometry, using linear regression to identify and remove outliers from the data set. There were 826 successful observations across all seven filters for both stars. The resulting catalogs of photometric data were used to calculate the corresponding synthetic photometry in Section 3.2..

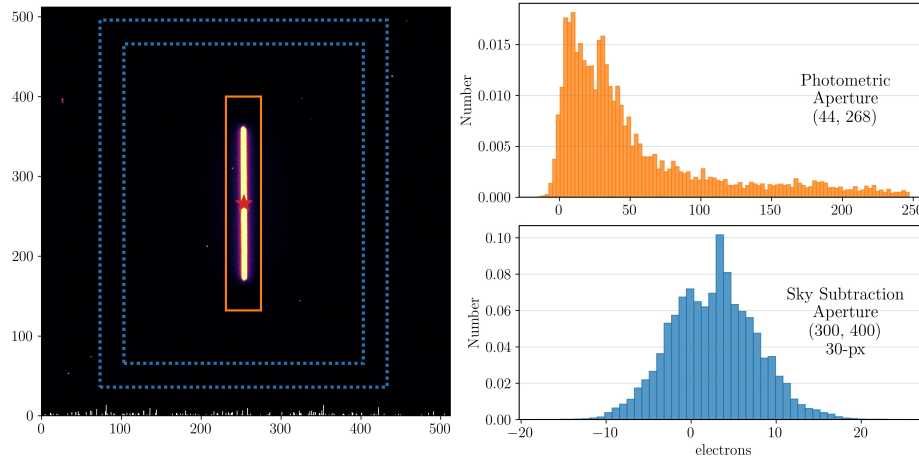


Figure 1: On the left is a spatial scan (HST observation ID idda02b0q) with a total exposure time of 59.9 seconds; outlined are the photometric aperture (solid orange lines) and the sky aperture (dotted blue lines). On the right are two histograms - the top corresponds to the pixel values (in units of electrons) in the photometric aperture while the bottom corresponds to the pixel values (in units of electrons) in the sky background aperture, corrected for a low-current, 12-electron additional post-flash.

3. Methods

Here we describe the steps of our novel method to calculate scan aperture corrections (Section 3.1.) and synthetic photometry catalogs (Section 3.2.).

3.1. Aperture Corrections

Due to their extended and linear nature, spatial scans cannot be represented by a straightforward empirical PSF in staring mode. In this section, we describe our method of creating SSFs for evaluating aperture corrections that are leveraged to compute absolute photometry of spatial scans.

To construct a SSF, we first build a PSF representing a star as observed in staring mode (Section 3.1.1). Then, that PSF is convolved with a line corresponding to the length and position of the scan trajectory on the CCD subarray (Section 3.1.2). The resultant SSF is then used to calculate the amount of flux enclosed by the rectangular aperture used to perform photometry on the spatial scans. The ratio between this amount and the total flux of the SSF is the enclosed energy fraction (Section 3.1.3).

3.1.1 Point Spread Functions (PSFs)

Two types of PSFs were built, which we call $\text{PSF}_{\text{simple}}$ and $\text{PSF}_{\text{blended}}$. Both PSF types were built with a 150-pixel radius (corresponding to 6 arcsec on the WFC3/UVIS pixel scale) and used published 1-dimensional UVIS encircled energy tables (see Deustua et al. 2017 and Calamida et al. 2021), which were radially expanded into 2 dimensions. The $\text{PSF}_{\text{blended}}$ category includes a 2-dimensional empirical PSF, derived from combining many exposures of bright stars acquired on-orbit (Anderson et al., 2015), inside a radius of 100 pixels, thus replacing the encircled energy values. Figure 2 compares the three types of PSFs (empirical, simple, and blended) for F275W.

$\text{PSFs}_{\text{simple}}$ were constructed for seven filters and both UVIS chips by taking the published, chip-dependent encircled energy (EE) values (Calamida et al., 2021), interpolating them to a radius of 150 pixels, and extrapolating the 1-dimensional profile into a circle. These EE values are derived from a large number of observations of standard stars. Note that for F275W and F814W, the values were updated in 2020 to correct for changes in the detector sensitivity before combining the individual exposures used to compute the encircled energies (see Calamida et al. 2021).

$\text{PSFs}_{\text{blended}}$ began with provided UVIS 2 PSFs derived from empirical observations (Anderson et al., 2015), and were constructed for five filters. As seen in the first plot of Figure 2, the empirical PSF only extends to 100 pixels in radius, so we spliced it with the $\text{PSF}_{\text{simple}}$ for the given filter at the 100-pixel boundary, and re-normalized to achieve continuity in the radial profile and total flux. Note that empirical PSFs for any UVIS 1 filters, as well as F218W and F225W on UVIS 2, are not yet available.

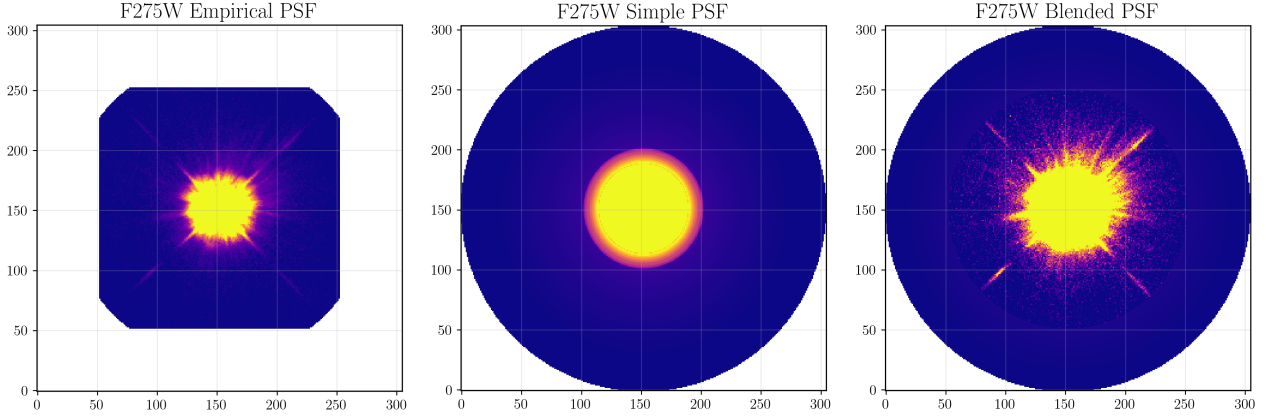


Figure 2: A comparison of F275W point spread functions utilized in this work. At left is the empirically derived PSF, which has a radius of 100 pixels. In the center is the $\text{PSF}_{\text{simple}}$, derived from the published encircled energy curves and assuming 100% flux at a 150-pixel radius. At right is the $\text{PSF}_{\text{blended}}$, which is created by splicing the empirical PSF to $\text{PSF}_{\text{simple}}$ at a 100-pixel radius. The empirical PSF component is renormalized under the assumption of 100% flux encapsulated at a radius of 150 pixels.

3.1.2 Scan Spread Functions (SSFs)

At a constant speed of 0.125 arcsec/second for a total exposure time of 59.900002 seconds, the observed scan trajectory on the WFC3/UVIS CCDs is 192 pixels long. We convolved each PSF with a 192-pixel-long line at an angle of 90.3° , thus producing filter-dependent SSFs for both PSF types ($\text{PSFs}_{\text{simple}}$ and $\text{PSFs}_{\text{blended}}$). Each phase of this transformation is shown in Figure 3 for F275W.

Note that the initial staring mode PSFs (left column of Figure 3) have dimensions of 302 by 302 pixels. Meanwhile, the scan trajectory and scan spread functions have dimensions of 512 by 512 pixels, to match the dimensions of the subarrays used in the actual photometric calibration scans (for details on subarray choice, see Section 2.1.).

3.1.3 Calculating Enrectangled Energy Fractions

For every SSF generated, the median simulated flux of the sky background rind pixels was calculated. Then, we subtracted that median flux level from the simulated flux of each SSF pixel in a rectangular photometric aperture identical to that used to perform photometry on observed scans. Finally, we measured the total simulated, sky-subtracted flux enclosed in the photometric aperture of the SSF. This enclosed energy should represent the true ratio of actual flux captured in the photometric aperture after sky background subtraction has been performed to the total flux emitted by an observed spatial scan.

The apertures used in Marinelli et al. (2022) (Figure 1) and thus employed for the aperture correction calculation are centered relative to either the observed scan or scan spread function, and are defined as follows:

- Photometric aperture: width of 44 pixels, height of 268 pixels
- Sky background aperture: 30-pixel-wide rind with an inner boundary of width 300 pixels and height 400 pixels and an outer boundary of width 360 pixels wide and height 460 pixels

As detailed in Marinelli et al. (2022), these apertures were selected after testing which values optimize the signal-to-noise ratio of the scans.

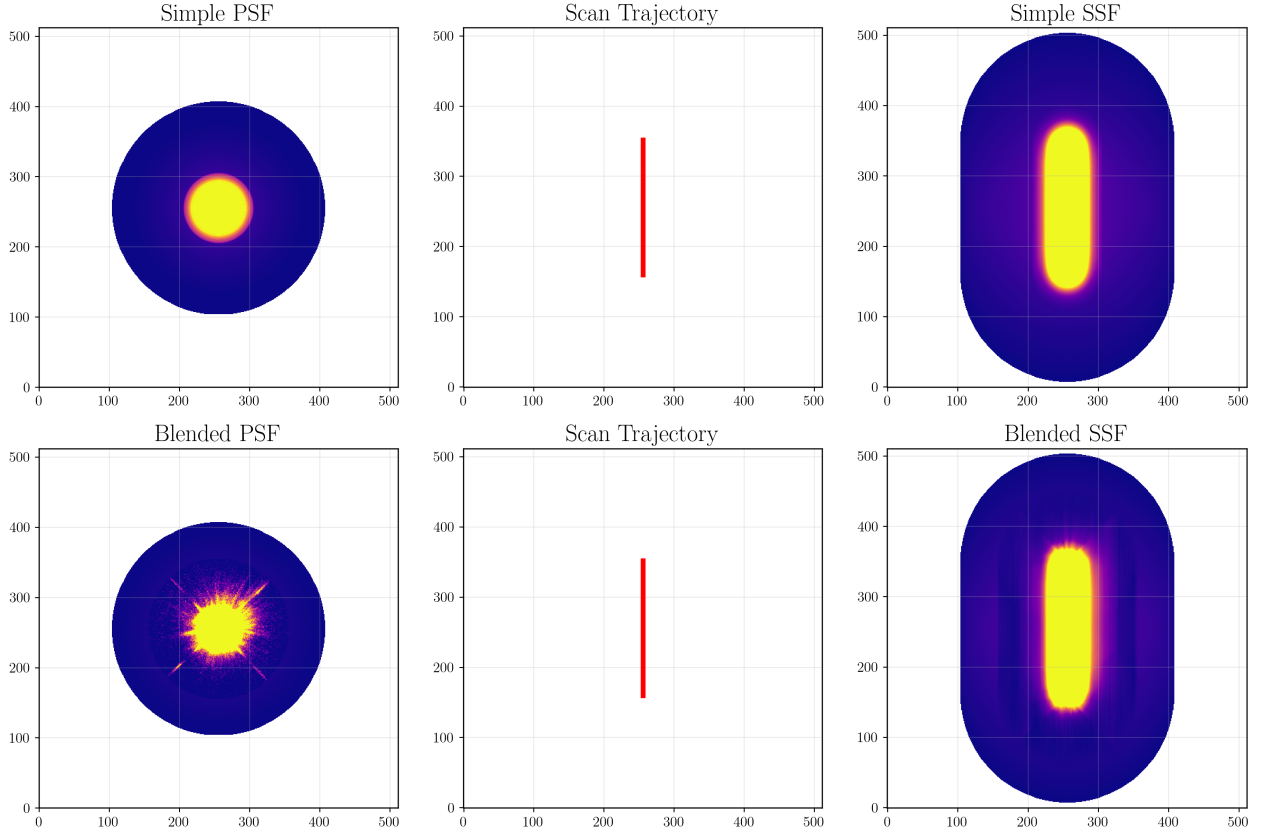


Figure 3: Demonstration of how a PSF (left column) is convolved with a trajectory line (middle column) to product a SSF (right column). The top row represents the “simple” models, which are derived from published encircled energy curves, while the bottom row represents the “blended” models, created from combining the aforementioned encircled energies with an empirical PSF.

An underlying assumption is that the photometric aperture encompasses almost all of the flux from the scan or SSF. Indeed, the PSFs with which we build our SSFs are normalized to a value of 1.0 at a 150-pixel radius. Convolution of a radially symmetric PSF with a 192-pixel-long line therefore results in an oval shape with a minor axis of 150 pixels and a major axis of 492 pixels, since the full PSF essentially emanates from the ends of the scan.

Figure 4 demonstrates the difference in calculated enrectangled energy based on three apertures, each with a different width (12, 20, and 44 pixels). As aperture width increases,

the enrectangled energy fraction in that aperture logically increases. It can be seen that the three ultraviolet filters are particularly sensitive to changing aperture width.

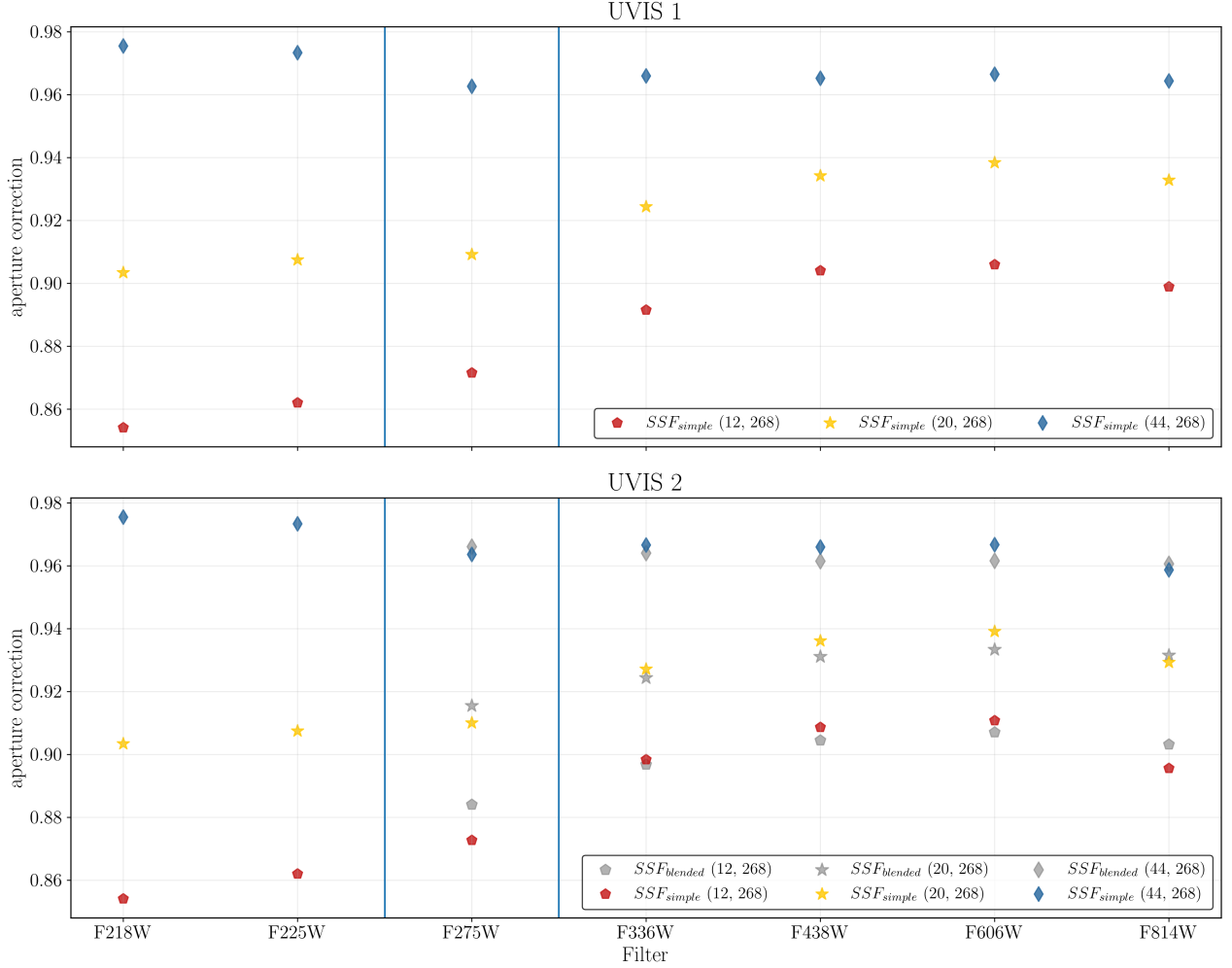


Figure 4: A comparison of the calculated rectangular aperture corrections for two sets of models, SSF_{simple} (colorful points) and $SSF_{blended}$ (gray points), and three apertures: all 268 pixels tall, and 12 (red), 20 (yellow), and 44 (blue) pixels wide. Top: UVIS 1. Bottom: UVIS 2.

Aperture corrections for $SSF_{blended}$ are marked as gray stars in the bottom (UVIS 2) panel of Figure 4, while the SSF_{simple} are indicated by colorful pentagons. Note that there are some differences in the performance of the two SSF model types in the five common filters. In F275W and F814W, the photometric aperture captures a slightly larger fraction of flux in the $SSF_{blended}$ compared to SSF_{simple} ; this effect is most noticeable at small apertures. Meanwhile, in F336W, F438W, and F606W, SSF_{simple} have a slightly larger enrectangled energy fraction than $SSF_{blended}$. As expected, the largest aperture width captures a significantly larger amount of flux than the smaller apertures. At 44 pixels wide, the two SSF methods agree relatively well and are able to capture a similar percentage of the

light across all filters. This validates the determination from Marinelli et al. (2022) that the 44-pixel-wide photometric aperture is sufficiently wide enough when compared to smaller apertures.

A small amount of flux at the ends of both the SSFs and the actual scans is enclosed by the background aperture, making a median background sky subtraction essential. This is unavoidable due to size of the subarray, the length of the scan trajectory, and the inherent spread of light from the scans. The inner and outer dimensions of the sky background rind were carefully engineered to maximize signal-to-noise. Observed scans are not always perfectly centered on the subarray; while careful steps are taken to ensure that scans affected by failed pointings or loss of gyro lock/control are not used, on occasion a scan is slightly vertically offset relative to the center of the 512×512 subarray, but data quality is otherwise unaffected. Increasing the inner dimensions of the sky background rind is not practical, as doing so would risk encapsulating more pixels at the edges of the subarray, where the performance of the cosmic ray rejection algorithm is poorest.

3.2. Synthetic Photometry

For each observed spatial scan, we calculated the corresponding time-dependent synthetic photometry, corrected for a rectangular aperture 44 pixels wide and 268 pixels long. This was achieved using the Python packages `synphot` and `stsynphot` under the following procedure:

1. From the actual scan observation, the following properties are extracted:
 - Target name (GD153 or GRW70)
 - Filter
 - Observation date
 - CCD (UVIS 1 or UVIS 2)
2. A UVIS 1 bandpass is constructed, using the given filter and observation date. Figure 5 shows the UVIS 1 bandpass for F275W.
3. The synthetic spectrum corresponding to the target is generated from the following CALSPEC models:
 - GD153: `gd153_stiswfcnic_003.fits`
 - GRW70: `grw_70d5824_stiswfcnic_003.fits`

See Figure 5 for a comparison of the synthetic spectra and an sample UVIS 1 bandpass range and throughput.

4. The synthetic spectrum is multiplied by the appropriate “enrectangled energy”, as determined by the UVIS CCD, filter, and desired SSF type. See Section 3.1. for an in-depth explanation of how the aperture correction was calculated.
5. A synthetic observation is built using the bandpass and the aperture-corrected spectrum.

6. The predicted count rate of the synthetic observation is calculated using the built-in `countrate` method and the known telescope collecting area.

The WFC3 calibration pipeline, `calwf3`, scales UVIS 2 observations by the ratio of the inverse sensitivities between the two detectors, as determined from the average of several standard stars (including GD153 and GRW70).⁵ In comparison, `synphot` does not apply the same ratio because we are computing the observation of a single star. For this reason, we used only UVIS 1 bandpasses, even for the construction of synthetic observations on UVIS 2.

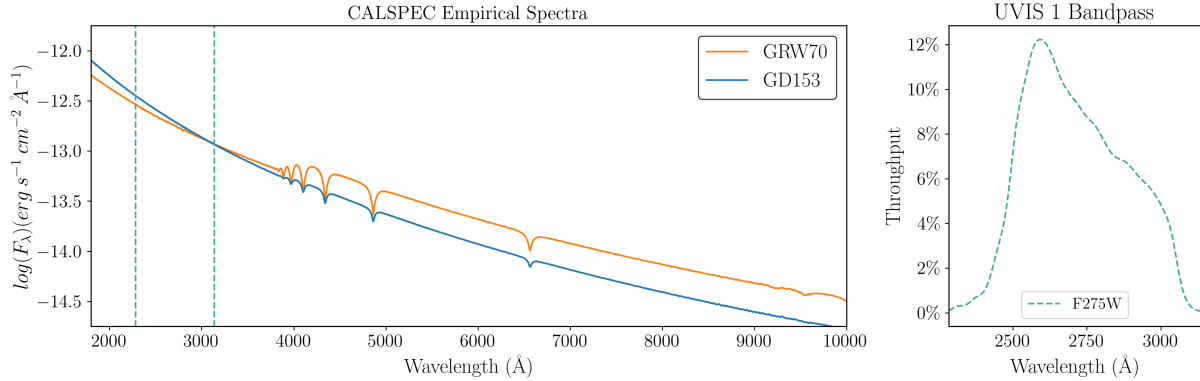


Figure 5: CALSPEC empirical spectral energy distributions for two spectrophotometric standard white dwarfs used in this work, compared to the total system throughput of the F275W UVIS 1 bandpass, used for the synthetic observations.

4. Analysis

4.1. Applying Aperture Corrections

As detailed in Section 3.2., we used the target, detector (chip), filter, and observation date of each observed scan to calculate a corresponding synthetic observation and count rate. The aperture correction as calculated in 3.1.3 is applied to the synthetic spectrum as a multiplicative factor, thus scaling the theoretical flux to what would be expected for a scan rather than a staring mode observation.

We then calculated the observed-to-synthetic ratios by dividing the observed count rate by the synthetic count rate. A lack of observable slope in the resulting data points with regard to time would validate the accuracy of the time-dependent zeropoints that are currently implemented in the `synphot` and `stsynphot` pipelines. Accuracy of the PSF and SSF models, as well as the appropriateness of our methodology, can be evaluated via any difference in the ratio from 1.0.

⁵As `calwf3` is part of the `hstcal` package, see the `hstcal` v1.0.0 Release Notes for details regarding the flux-scaling of UVIS 2.

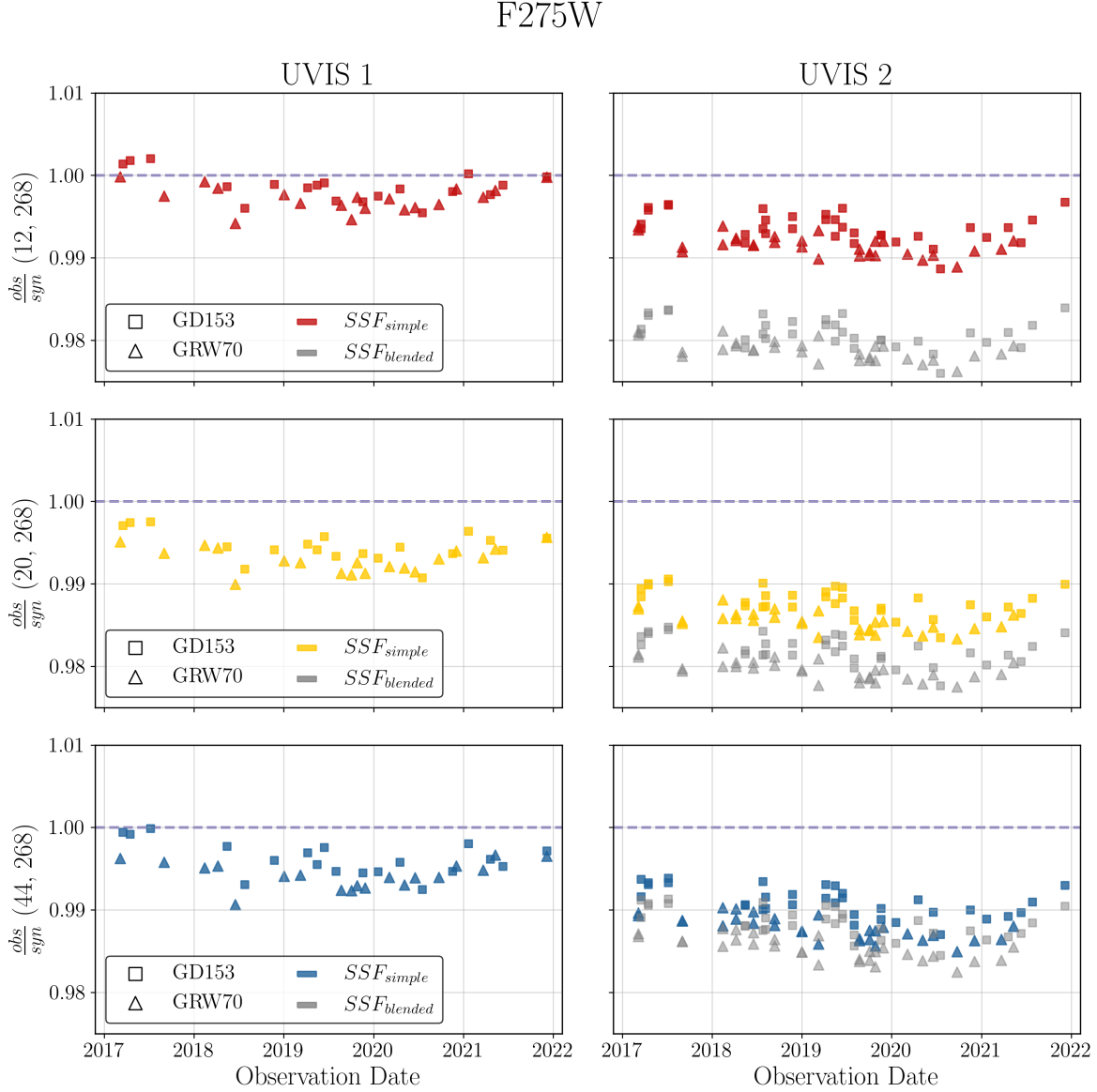


Figure 6: Comparison of photometric observed-to-synthetic flux ratios for F275W on UVIS 1 (left) and UVIS 2 (right), employing three different rectangular apertures for both the observed photometry and the aperture correction for the synthetic observation. These three apertures are all 268 pixels in height, and have widths of 12 (red; top row), 20 (yellow; middle row), and 44 (blue; bottom row) pixels.

4.2. Effect of Aperture Width

We return to the enrectangled energies calculated for different aperture widths as presented in Figure 4. In Figure 6, we apply these enrectangled energies to the F275W photometry. For each aperture width, both observed photometry and aperture corrections were calculated and the ratio of observed-to-synthetic count rate taken.

The smallest aperture (12 pixels wide, top panel) results in observed-to-synthetic ratios that are closest to 1 for both CCDs. The medium aperture (20 pixels wide) results in observed-to-synthetic ratios that are the farthest offset from 1. The largest aperture (44 pixels wide), which is employed for the rest of this report, results in ratios that are slightly closer to 1 than the 20-pixel aperture. However, values are still offset, most significantly on UVIS 2. Furthermore, the $\text{SSFs}_{\text{blended}}$ had a greater offset than the $\text{SSFs}_{\text{simple}}$. The $\text{SSFs}_{\text{blended}}$ resulted in slightly poorer results at smaller radii, possibly indicating an issue with the implementation of the empirical PSF. However, $\text{SSFs}_{\text{blended}}$ and $\text{SSFs}_{\text{simple}}$ agree to within $\approx 0.5\%$ for the largest aperture.

5. Results

We find that within each filter and chip combination, the mean observed-to-synthetic flux ratios are tightly clustered and are close to 1.0, with the exception of the UV filters, where the observed photometry is $\approx 2\%$ fainter than the synthetic values (Figures 8 and 9). With one exception (UVIS 1 in the F606W filter), there is no positive or negative slope easily fit to the data, validating the time-dependent zeropoints as implemented in the `synphot` and `stsynphot` packages.

There appears to be a wavelength-dependent systematic offset in the observed-to-synthetic ratios for UVIS spatial scans, tabulated in Table 2, plotted in Figure 7, and included in the labels for Figures 8 and 9.

CCD	Filter	Mean Offset	CCD	Filter	Mean Offset
UVIS 1	F218W	-1.87%	UVIS 2	F218W	-2.98%
	F225W	-1.21%		F225W	-2.33%
	F275W	-0.43%		F275W	-0.94%
	F336W	-0.59%		F336W	-0.67%
	F438W	0.11%		F438W	-0.44%
	F606W	$0.88\%^*$		F606W	0.11%
	F814W	0.49%		F814W	0.16%

Table 2: Calculated mean offsets of the observed-to-synthetic flux ratios, as derived from $\text{SSFs}_{\text{simple}}$, representing the percentage difference between the calculated observed photometry and the aperture-corrected synthetic count rate.

*Note that the UVIS 1 F606W offset represents the mean of a set of time-dependent data, as seen in the sixth subplot of Figure 8: the earliest data is less than the mean offset while the latest data is greater than the mean offset. This is the anticipated result of imperfect sensitivity change parameterization for this filter on UVIS 1 (at the $\approx 0.5\%$ level); see Marinelli et al. (2022) Figures A53 and A54 to compare the F606W relative photometric sensitivity changes between CCDs since 2009.

As seen most clearly in Figure 7, the mean observed-to-synthetic ratio within each filter on each CCD increases with wavelength. Filter F336W has the closest agreement between CCDs, as the UVIS 1 mean is only 0.08% greater than the UVIS 2 mean. Filter F814W

also has relatively good agreement between CCDs, with only 0.33% difference between the mean ratios. The filters in which there is the best agreement between the observed and synthetic count rates are F438W, F606W (UVIS 2 only), and F814W. In the UV filters F218W, F225W, and F275W we see the greatest disagreement both between the observed and synthetic count rates, as well as between the two CCDs.

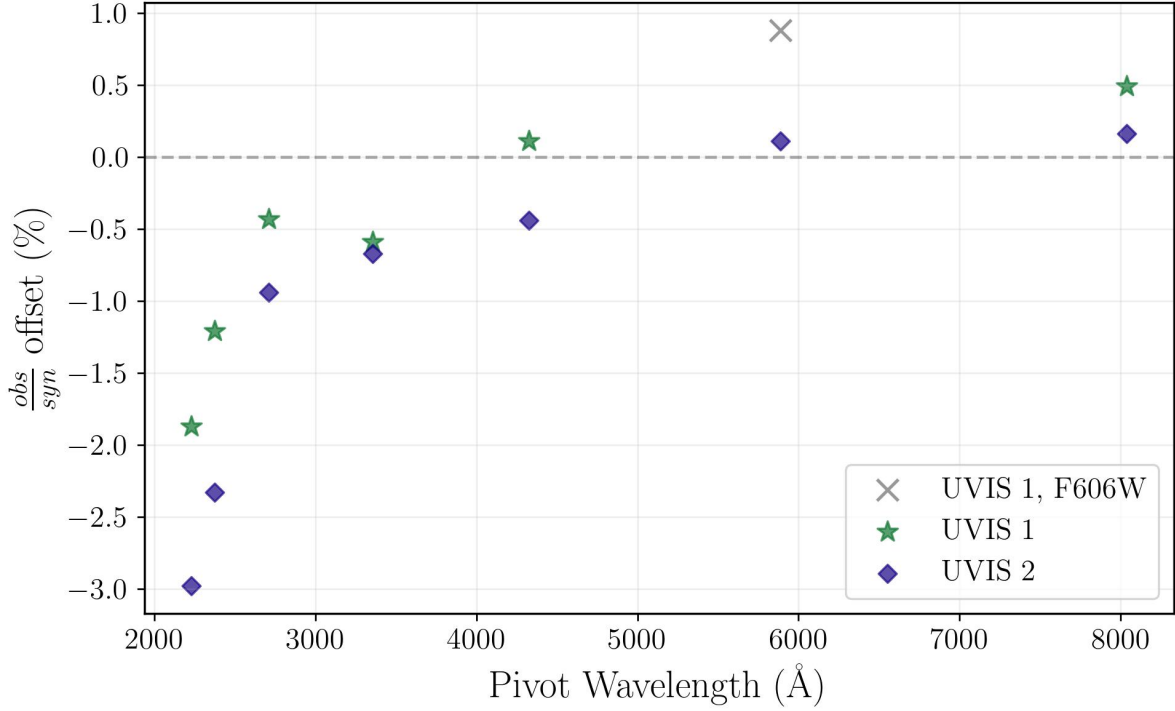


Figure 7: Calculated offset of the observed-to-synthetic count rates, as a percentage, plotted against the pivot wavelength of the filter. UVIS 1 points (with one exception) are marked with green stars and UVIS 2 points are marked with indigo diamonds.

Unlike the offsets for the other filter/CCD combinations, the UVIS 1 F606W mean offset is not representative of the entire dataset (see the caption of Table 2 for more details). Accordingly, while we include it here for completeness, it is marked with a gray “x”.

It is likely that there are multiple underlying systematic factors pushing the observed-to-synthetic ratios in different directions, and thus we refrain from making any claims regarding the accuracy of our PSF and SSF models at this time. Until we fully understand the discrepancies in our models and data and the offsets are resolved, scans cannot be used for directly computing zeropoints.

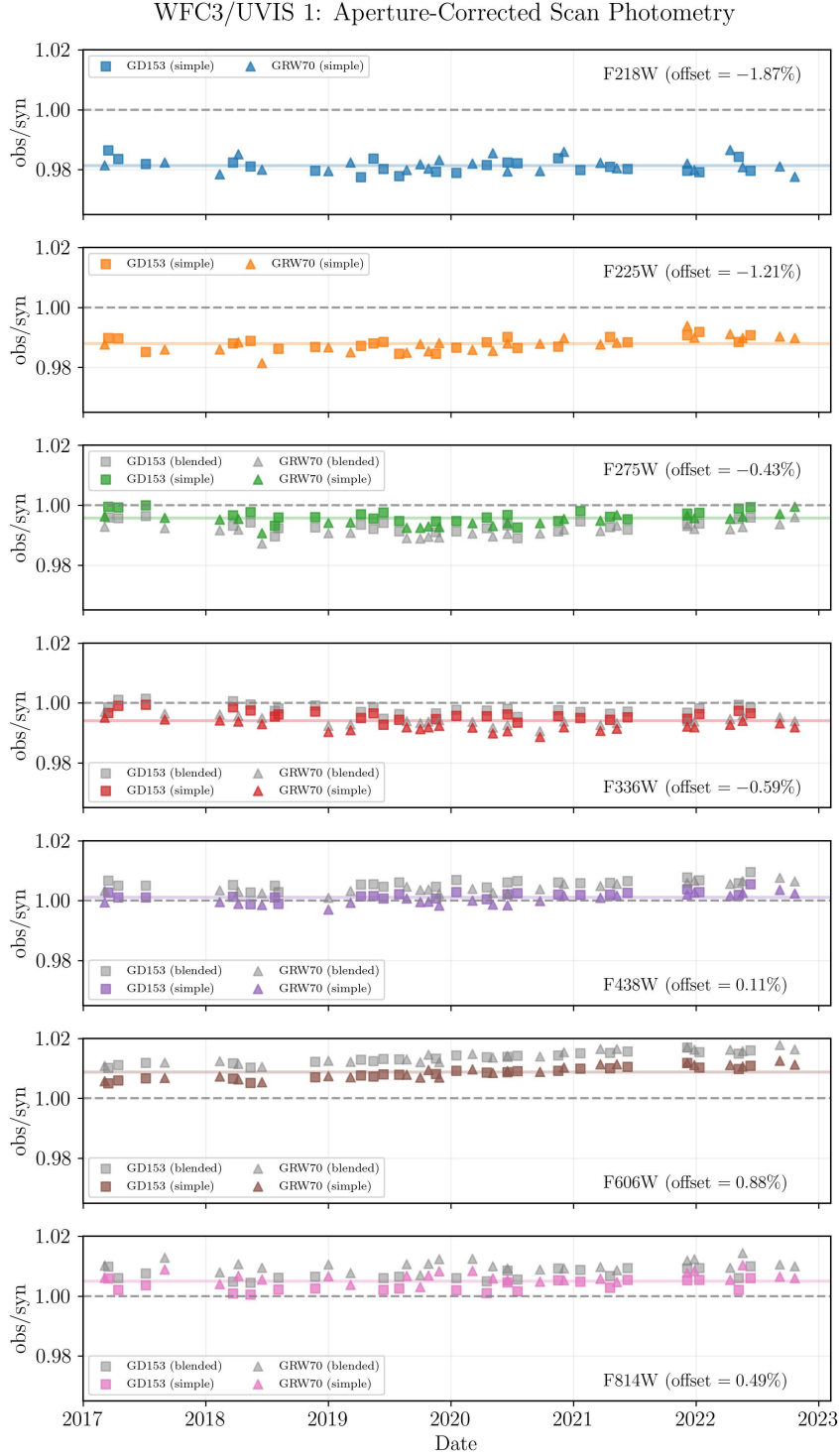


Figure 8: Observed-to-synthetic flux ratios for UVIS 1 spatial scan photometry in seven wide filters. Colorful points denote the usage of $\text{SSFs}_{\text{simple}}$ to calculate aperture corrections, while gray points represent usage of $\text{SSFs}_{\text{blended}}$. GD153 data are square-shaped and GRW70 data are triangle-shaped. Each plot is labeled with the filter and mean offset from 1.0 for $\text{SSF}_{\text{simple}}$ -corrected ratios.

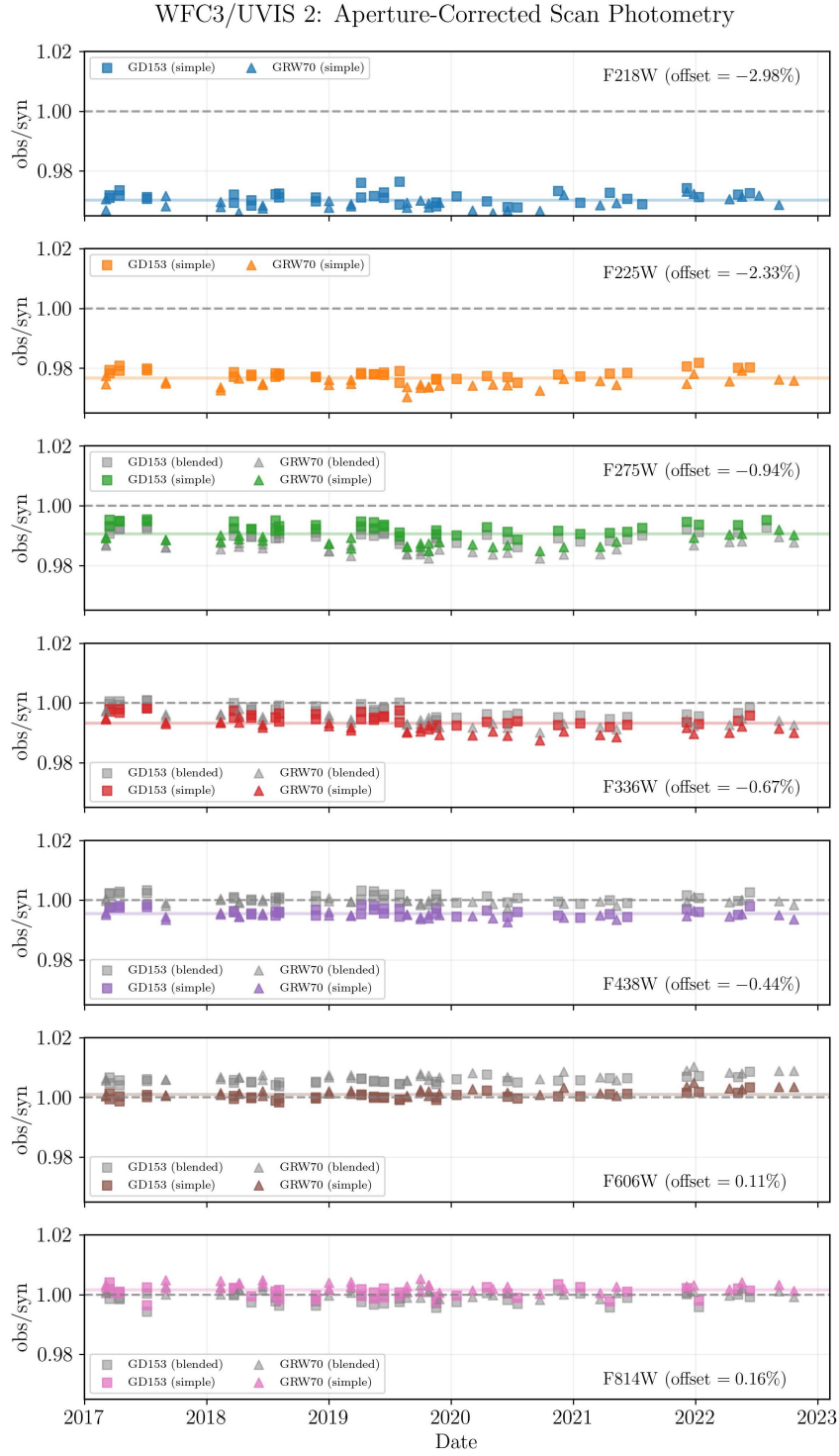


Figure 9: Like Figure 8, but for UVIS 2 spatial scans.

In this work, we make use of published encircled energy curves (Calamida et al., 2021). These are optimized for smaller radii and assume that 100% of the flux is enclosed within a radius of 6 arcsec, or 150 pixels. Indeed, we splice the empirical PSFs to the EE curve at 100 pixels - an action rooted not only in the assumption that the empirical PSFs are accurate to 100 pixels, but also the assumption that the published encircled energy values from 100 to 150 pixels are accurate.

Intriguingly, by analyzing the deep observations of isolated and saturated PSFs in F275W from calibration programs 11438 and 11919 designed to study the UVIS PSF wings (Figure 10), we find evidence suggesting that there may be 1 – 2% additional flux at distances greater than 6 arcsec. Additionally, Medina et al. (2022) suggest that the 2009 optical model, used in the encircled energy tables between 1.4 and 6 arcsec, may over-predict the encircled energy beyond 7500 Å. This effect is most prominent in the bluest UV filters (F218W and F225W), where the observed count rates were up to $\approx 2.5\%$ less than the synthetic count rate.

Together, these have significant implications for extended objects like spatial scans. If the current published encircled energy values are found to have underlying inaccuracies (especially at large radii), that could contribute significantly to the error budget.

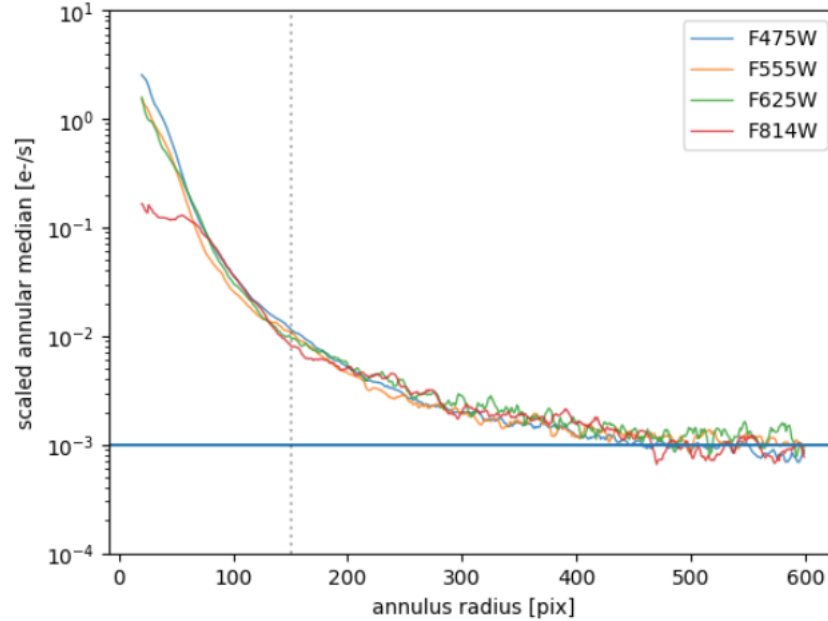


Figure 10: Median count rate values in annuli of increasing radii of selected isolated super-saturated stars for four filters: F475W, F555W, F625W, and F814W. Values are scaled to align the shape of the curves past after approximately 100 pixels. The dashed vertical line represents a radius at 150 pixels, and the solid blue horizontal line indicates an asymptotic value for the annular median. The shape of the curves indicate that there is flux from the PSF unaccounted for in an extended region past 150 pixels, as the flux continues to steadily decline between radii of 150 pixels and 400 pixels, whereas background light would be flat.

6. Discussion

Staring mode photometry, directly used to calculate the time-dependent zeropoints, has lower precision than spatial scan photometry (Marinelli et al., 2022). That the observed-to-synthetic spatial scan flux ratios lack a slope within the filter/chip configurations (with the known exception of UVIS 1/F606W) is a good validation of the appropriateness of the currently implemented zeropoints. However, the ratio around which scan observed-to-synthetic values is offset from 1.0 in most filters, up to a $\approx 3\%$ systematic difference between the observed photometry and aperture-corrected synthetic count rate.

We suspect our aperture corrections have multiple underlying systematic errors due to the normalization of the encircled energy curves and/or empirical PSF models used to make the convolution kernels. An additional source of error stems from possible inaccuracies in the published EE values at large radii.

To more thoroughly investigate the behavior of the UVIS PSF at large radii, we have designed a calibration observing program (Program 17271) which will take deep exposures of white dwarf standard stars in several of the core filters used in this report. This will enable the WFC3 Instrument Team to more accurately calculate the encircled energy at radii beyond 150 pixels (6 arcsec), as well as better understand the encircled energy from 35 to 150 pixels, where the chip-dependent encircled energies from direct images is spliced to an optical model for most UVIS filters (Hartig 2009; Medina et al. 2022).

These issues impact spatial scans more than staring mode photometry due to the former’s high precision nature and the large apertures. Since staring mode calibration of the UVIS detector is done with shorter exposure times and photometric and background apertures of smaller radii, we expect that differences in the EE at large radii would contribute negligible, if any, error.

7. Conclusions

In this report, we introduced a novel method for aperture correcting scan photometry for the WFC3/UVIS detector and presented preliminary results from applying the method to calibration scans of two white dwarf standard stars.

We summarize our major points as follows.

- Due to their extended linear morphology, scanning mode observations cannot be accurately modeled by radially-symmetric point-spread functions (PSFs) alone. Instead, we convolved PSFs with the scan trajectory on the subarray to create “scan spread functions” (SSFs).
- We created two sets of PSFs with 150-pixel (≈ 6 arcsec at the WFC3/UVIS pixel scale) radii:
 1. **PSF_{simple}** were generated from radially expanding EE values into two dimensions. A total of 14 were created, representing both CCDs and seven filters: F218W,

F225W, *F275W*, *F336W*, *F438W*, *F606W*, and *F814W*. UVIS 2 PSFs_{simple} in the italicized filters were also used in the creation of the second set of PSFs.

2. **PSF_{blended}** were created from combining 100-pixel radii empirical PSFs (Anderson et al., 2015) with the corresponding PSF_{simple} from 100 to 150 pixels. A total of five were created, representing the UVIS 2 CCD and five filters: *F275W*, *F336W*, *F438W*, *F606W*, and *F814W*.
- Treating the convolved SSFs identically to observed spatial scans, we measured the fraction of flux enclosed in a rectangular photometric aperture.
 - We generated catalogs of time-dependent synthetic observations, matched to the catalogs of observed photometry, and aperture corrected the expected count rate using the flux fraction as a multiplicative aperture correction.
 - Observed-to-synthetic scan flux ratios over time:
 - are essentially flat with no slope (with the exception of UVIS 1/*F606W* which has a known imperfect sensitivity correction at the 0.5% level that will be addressed in the near future). This is an additional validation of the implemented zeropoints, which are primarily based on staring mode observations, using only higher precision scanning mode observations; and
 - show a wavelength-dependent offset that differs between CCDs, indicating underlying systematic factors affecting the aperture corrections and/or photometric calculations with rectangular apertures.
 - There are indications that there may be 1 – 2% additional flux at greater than 150 pixels for the WFC3/UVIS PSF, which may be impacting results due to the extended nature and longer exposure times of spatial scans. An upcoming calibration program will make deep observations of isolated stars to better understand the UVIS PSF at large radii, which we hope will help improve aperture corrections for spatial scans.

Acknowledgements

We thank Annalisa Calamida and Jennifer Mack both for their extensive review of this ISR and many valuable discussions regarding this work. Additionally, we are grateful to Catherine Martlin and Sylvia Baggett for reviewing this report and providing helpful feedback. We also thank Joel Green for his thorough editorial review.

References

- Anderson, J. 2020, Strategies for Mitigation of CTE Losses in WFC3/UVIS, Instrument Science Report WFC3 2020-8, 10 pages
- Anderson, J., Baggett, S., & Kuhn, B. 2021, Updating the WFC3/UVIS CTE model and Mitigation Strategies, Instrument Science Report 2021-9, 44 pages
- Anderson, J., Bourque, M., Sahu, K., Sabbit, E., & Viana, A. 2015, A Study of the Time Variability of the PSF in F606W Images taken with the WFC3/UVIS, Instrument Science Report WFC3 2015-08, 19 pages
- Bohlin, R. C., Hubeny, I., & Rauch, T. 2020, AJ, 160, 21, doi: 10.3847/1538-3881/ab94b4
- Calamida, A., Mack, J., Medina, J., et al. 2021, New time-dependent WFC3 UVIS inverse sensitivities, Space Telescope WFC3 Instrument Science Report 2021-04
- Deustua, S. E., Mack, J., Bajaj, V., & Khandrika, H. 2017, WFC3/UVIS Updated 2017 Chip-Dependent Inverse Sensitivity Values, Space Telescope WFC3 Instrument Science Report 2017-14
- Hartig, G. F. 2009, WFC3 SMOV Programs 11436/8: UVIS On-orbit PSF Evaluation, Instrument Science Report WFC3 2009-38, 12 pages
- Kalirai, J. S., Cox, C., Dressel, L., et al. 2010, WFC3 Pixel Area Maps, Instrument Science Report WFC3 2010-08, 7 pages
- Lim, P. L. 2018, stsynphot, 0.1.1, Zenodo, doi: 10.5281/zenodo.3247832
- . 2020, synphot, 1.0.1, Zenodo, doi: 10.5281/zenodo.3971036
- Marinelli, M., Bajaj, V., Calamida, A., et al. 2022, Monitoring WFC3/UVIS Photometric Sensitivity with Spatial Scans, Instrument Science Report WFC3 2022-4, 80 pages
- McCullough, P. 2017, Trajectories of Multi-lined Spatial Scans, Space Telescope WFC3 Instrument Science Report 2017-06
- Medina, J., Mack, J., & Calamida, A. 2022, WFC3/UVIS Encircled Energy, Instrument Science Report WFC3 2022-2, 23 pages
- Riess, A. G., Casertano, S., Yuan, W., et al. 2018, ApJ, 855, 136, doi: 10.3847/1538-4357/aaadb7
- Shanahan, C., McCullough, P., & Baggett, S. M. 2017, Photometric Repeatability of Scanned Imagery: UVIS, Space Telescope WFC3 Instrument Science Report 2017-21